Fabrication of tin-based halide perovskites by pulsed laser deposition

Sarah Hoffmann-Urlaub[1] · Yaodong Zhang[1] · Zhaodong Wang[1] · Birte Kressdorf[1] · Tobias Meyer[2]

Abstract

Mixed-organic-cation perovskite absorbers as formamidinium doped methylammonium tin iodine $(NH_2CH)_{1-x}(CH_3NH_3)_xSnI_3$ ($x \leq 1$) can provide a pathway to highly efficient lead-free solar cells. Although this class of materials is known to be severely susceptible to degradation, induced among others by enhanced temperatures, humidity and illumination, an improved layer quality in view of crystal size and homogeneity is the key to diminish or even to block certain degradation channels. In this work, we present the fabrication of fully tin-based perovskites via pulsed laser deposition. The morphology is analyzed for different deposition energies and temperatures to find the optimum process window. The thin films already reveal crystalline structure at room temperature, while they are smooth and homogeneous above a critical thickness for carefully adapted deposition parameters. In contrast to the assumption that at elevated temperatures, the crystallinity is improved, and we find that the films reveal a strong organic depletion and simultaneously tin enrichment. As a measure for their suitability to be employed as photovoltaic absorbers, the band gap of the differently doped perovskites is estimated by spectroscopic ellipsometry in the range of 1.3 to 1.4 eV.

Keywords Lead-free organic-inorganic halides · Pulsed laser deposition · Mixed-cation tin perovskites · Ellipsometry · Solar cells

1 Introduction

Thin film hybrid organic–inorganic perovskite (HOIP) solar cells were identified to be a suitable alternative to conventional Si-cells, since they are cheap, scalable and fabricated from abundant materials. In terms of light-harvesting properties, they are capable to even exceed the latter in view of power conversion efficiency (PCE) due to their higher theoretical Shockley–Queisser limit of 30.5% [11]. The most important component is the absorber layer that consists of a metal halide in perovskite structure, where metals from group IV (Ge, Sn and Pb) and organic complexes as methylammonium iodine (MAI) and formamidinium iodine (FAI) are frequently used. These complexes reveal exceptional photovoltaic properties due to a balanced transport of electrons and holes, high absorption coefficients [44], direct and tunable band gaps [36] and long carrier diffusion lengths [32, 45]. Hence, a lot of effort was put in developing perovskite solar cells, resulting in an increase of PCE from 3.8 to 25.2% [52] within a few years.

However, record breaking cells of this class of highest PCE simultaneously reveal lead toxicity [2]. Recently, it became apparent that replacing lead by tin is a promising approach to circumvent this problem [18]. Nonetheless, the stability under illumination and humid conditions of the absorber material is still an unsolved issue [28] that currently limits their usage to the bench scale. For the most part, performance instability and degradation in HOIPs can be attributed to ion migration and decomposition of the lattice structure due to illumination or exposure to moisture [23]. In detail, it is assumed that photo-generated holes react with iodide in the perovskite lattice forming a vacancy and a neutral iodine transferred to the interstitial lattice. This way more iodine is excorporated from the lattice than tolerable in equilibrium, potentially leading to decomposition of the perovskite structure and hence loss of the directly coupled characteristic properties. An approach to block this governing degradation channel is to add surplus iodine to

✉ Sarah Hoffmann-Urlaub
shoffma3@gwdg.de

1   Institute of Materials Physics, University of Göttingen, Friedrich-Hund-Platz 1, 37077 Göttingen, Germany

2   4th Institute of Physics - Solids and Nanostructures, University of Göttingen, Friedrich-Hund-Platz 1, 37077 Göttingen, Germany

the perovskite structure to occupy the interstitial sites. For the fabrication of layers in a non-equilibrium state, conventional fabrication procedures like spin- or spray-coating [6] cannot be employed. Thus, vapor-based techniques such as pulsed laser deposition (PLD) can give access to deposit layers under such conditions.

In 2015, it was first demonstrated that metal-halide lead and tin-based films can be grown by PLD [4]; hence, in this work extensive characterizations of lead-free films are presented, where several targets with a substantially increased amount of the organic component are used, since the latter is known to be reduced in thin films compared to the target stoichiometry. For PLD grown lead-containing cells, a PCE of 10.9% was reached from a standing start [5], while hysteresis in current–voltage measurements was still observed due to charges trapped at internal interfaces such as grain boundaries [24] or ferroelectric polarization in the perovskite [10]. In detail, many/small grain boundaries/sizes limit the carrier diffusion lengths [32] and hence shorten their lifetime [14], because they act as pinning centers and foster recombination of differently charges species [40]. Therefore, in a next step an essential prerequisite is smooth and homogeneous thin films.

It was shown that with mixing FA and MA, the film morphology is improved [53], the charge carrier recombination [9] and the extent of Sn oxidation are notably reduced, and also the new structure is more sensitive to water absorption [48]. This compositional engineering incidentally leads to a strengthening of the thermal stability [8, 20]. This is even more convenient, considering that during operation the temperature of solar cells can easily exceed 100 °C. In this range, reversible phase transitions of the crystal structure have been reported in the absorber material [3], which can affect the photovoltaic performance due to their direct impact on the band structure. Furthermore, as a consequence of diffusion for thermally activated processes, irreversible changes are expected to happen. These can even be beneficial for photovoltaic devices, since crystallinity, grain size and continuity of the film can be enhanced as a result of low-temperature treatment ($T < 100\,°C$) [7, 15].

In generic ABX_3 perovskites, the A cations (here MA^+ or FA^+) are located in the middle of a (cubic) unit cell and the B cations (Sn^+) occupy the corner sites, surrounded by an octahedron of X anions. To pre-estimate, whether a certain combination of ions exhibits perovskitic structure, the tolerance factor t can serve as a measure [16]. Here, the effective ionic radii for the A and B cations r_A and r_B, respectively, are related to the anionic radius r_X by $t = (r_A + r_X)/[\sqrt{2}(r_B + r_X)]$. Values $0.8 \leq t \leq 1.0$ denote that a perovskite is formed, while for a cubic structure $t \geq 0.9$ is required. For components used in this paper, the tolerance factors are $t = 0.922$ (MA) and $t = 0.998$ (FA) [38]. Although for MA and FA various crystal structures

have been reported at room temperature [12], here the pure perovskites both reveal cubic structure [42] as well as their mixture.

In this work, we present the deposition conditions where metal-halide perovskites with different cation mixtures can be fabricated by PLD technique. Furthermore, we investigate the effect of the deposition temperature in comparison with room temperature deposition in regard to improvement in smoothness and crystallinity. The suitability of the PLD fabricated films for applications in photovoltaics is checked by evaluating the band gaps.

2 Experimental section

2.1 Target fabrication

The targets were fabricated from initial powders of SnI_2 (99.999% pure, Sigma-Aldrich), MAI ($\geq$ 99% pure, Sigma-Aldrich) and FAI ($\geq$ 99% pure, Sigma-Aldrich). The powders were weighed according to their molar ratios. Two targets with an equal amount of organic and inorganic components, one target with a fourfold and one with an eightfold enhanced organic portion, were fabricated (see Table 1).

Each of the mixtures was homogenized by manual milling in a glovebox under argon atmosphere. Afterward, the reactants were heated in a glass tube to 200 °C for 2 h (targets I–III) or 160 °C for 2.5 h (target IV), respectively, in order to initiate the solid-state transformation.

Finally, the reaction product was compressed into a compact pellet by 120 bar for 20 min (Fig. 1) that served as a target for pulsed laser deposition. The tin-to-iodine ratios are estimated in the compacted target.

2.2 Thin film deposition

The perovskite thin films were deposited by PLD on silicon (911) substrates, revealing no reflexions in XRD scans that may overlap with the ones of the thin films as it is the case for commonly used transparent conducting oxides such as ITO or FTO. Since the crystal growth of the thin film is not conveyed by any epitaxial relations but is governed by means

Table 1 Compositions of the four targets

Target	SnI_2	MAI	FAI	Sn/I ratio
I.	1	1	0	2.49
II.	1	0.2	0.8	2.64
III.	1	4 × 0.2	4 × 0.8	4.89
IV.	1	8 × 0.2	8 × 0.8	7.19

The listed values denote the moles per component and the Sn to I ratio given in atomic percentage, respectively
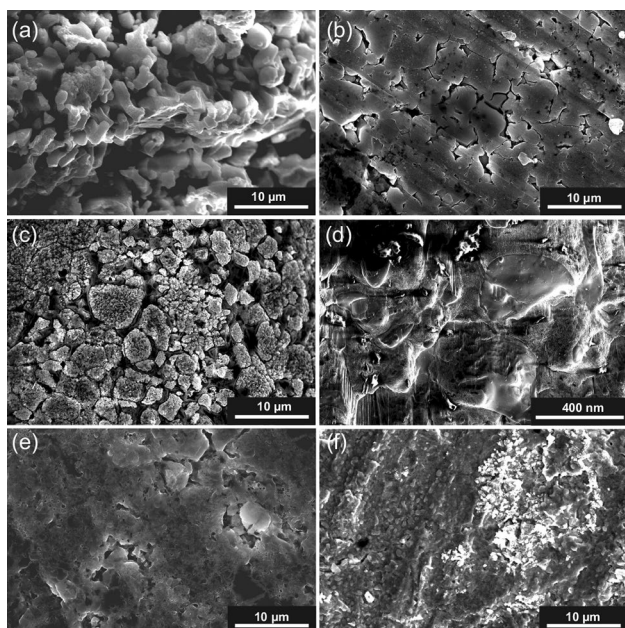
Fig. 1 SEM images of reacted powder of MAFASI (**a**) and the corresponding target II (**b**). Surfaces of the MASI target (I) after irradiation (**c**) and (**d**). **e** and **f** targets III and IV, respectively

of self-organization, the actual substrate type or lattice constant is of minor significance. Preference is given to silicon compared to quartz or glass due to the well-defined surface finish and purity, which excludes the impact of inhomogeneous interfaces and therefore allows to study only the perovskite properties. In case of PLD as deposition method, the substrate material is easily interchangeable as well as deposition of additional top or bottom layers required for complete solar cell devices in the future. A KrF excimer laser (COMPex 205F, Coherent) with a wavelength of 248 nm, a pulse duration of 30 ns and a repetition rate of 5 Hz was used. The background pressure in the vacuum chamber during the deposition was approximately 1.5×10^{-6} mbar. The substrate temperature was varied from 20 to 160 °C and the laser fluence from 0.16 to 0.41 J/cm^2 or the energy in the deposition chamber 80 mJ to 200 mJ, respectively. The laser spot size was kept constant throughout all experiments at 0.49 cm^2.

2.3 Characterization methods

X-ray diffraction (XRD, D8, Bruker) was used to analyze the crystallographic structure of targets and thin films. Here, angles between 10° and 70° were scanned, since for both cubic perovskites all characteristic features are visible in this range. A scanning electron microscope (SEM, Nova NanoSEM, FEI) was used to record images of the specimens surfaces. The same facility was used to analyze the chemical composition of the samples by energy-dispersive

X-ray spectroscopy (EDX). The accuracy of the EDX measurements is about 5%. The extraction of a lamella from the thin film for transmission electron microscopy (TEM) was conducted in an Helios G4 focused ion beam (FEI). In order to prevent damage at the sensitive surface, a platinum protection bar with several hundred nanometer thickness was deposited with the electron beam prior any ion beam impingement. The subsequent TEM measurements were taken in an Titan G2 80-300 (FEI) operated at 300 kV and equipped with a Gatan Quantum 965 ER image filter for electron energy loss spectrometry (EELS) and an X-Max 80 mm^2 detector (Oxford Instruments) for EDX data acquisition, respectively. Before integrating the EDX counts, a background subtraction was conducted using HyperSpy [13]. The film thickness was estimated by profilometry (Dektak 150, Veeco). The corresponding error is 10 nm. Optical properties were analyzed using an ellipsometry system (EP^3, Accurion) equipped with nanofilm_ep4 modelling software to model die dielectric functions from the two observables Δ and Ψ that were directly measured by the instrument.
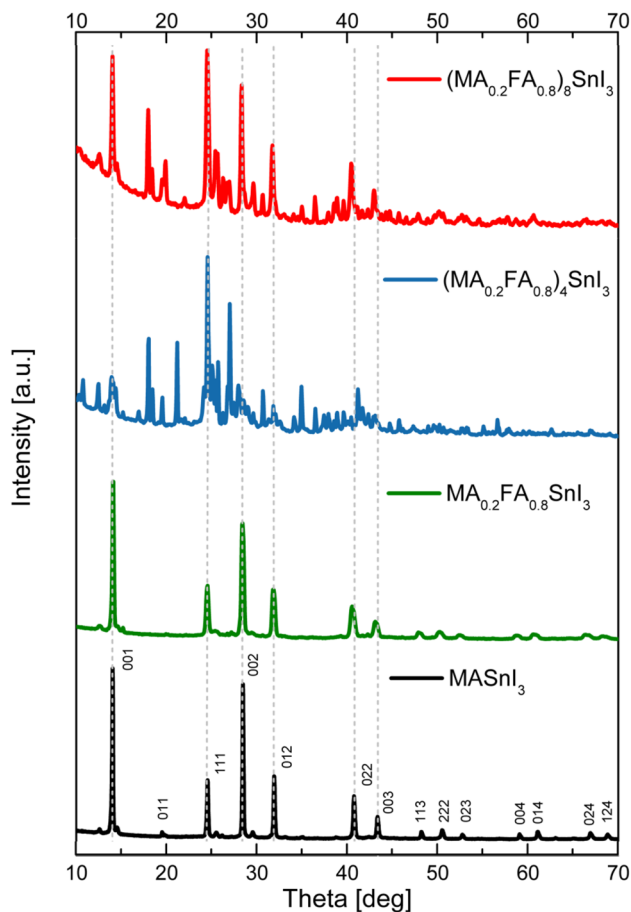
3 Results and discussion

3.1 Targets

The reacted powders for the $MA_{0.2}FA_{0.8}SnI_3$ (MAFASI) in Fig. 1a exhibit an open-cell-like structure consisting of cohesive crystallites with a diameter of approximately 3 µm and for the most part planar surfaces.

These features are still visible when the powders are compacted (b), while additionally crystallites with a size of a few hundred nanometers are present on top of the granular structure.

The general target structure is similar for the MASnI$_3$ (MASI) powder and pellet. The condition of an irradiated target is depicted in (c,d). The granular structure is intact, while the grain sizes are comparable to (a), but their surface shows extensive roughness. In detail, wavy facets of $SnI_{2-\delta} (\delta \leq 2)$ with a smooth shape and surface are formed. In these areas, the organic component is volatilized during the melting step of the laser ablation. The inorganic part remaining on the target surface reveals a morphology typical for a solidification process. This local inhomogeneity in the chemical composition is extended over time and can only be removed by polishing the target surface. Since this is only a surface-near phenomenon, neither the overall structure nor the composition of the target are affected. The targets of $(MA_{0.2}FA_{0.8})_4SnI_3$ (MAFA$_4$SI) and $(MA_{0.2}FA_{0.8})_8SnI_3$ (MAFA$_8$SI) are both composed of larger agglomerates and hence a higher densification but an enhanced porosity and number of crystallites, respectively, as well.

As a unique feature of the PLD technique, it is not mandatory to provide a target in the same structure for growing a film in a specific orientation, since the target material is evaporated during the process, dissolving most of the structural connections. Indeed the deposition of organics or polymers, respectively, is a special case, as the material is not split up into single atoms or at most atom clusters, but it is often found that the molecules or agglomerates are decomposed into fragments and transferred to the substrate [27, 29]. Hence, in the run-up to deposition it is inevitable to find the ideal the starting material leading to the desired composition on the substrate. In order to achieve this, we fabricated several targets with different ratios of the inorganic and organic part (see Table 1).

XRD is performed to monitor, whether the solid-state reaction was completed or if residuals of the initial powders remained. In Fig. 2, the diffractograms of the four fabricated targets are depicted, clearly revealing a cubic perovskite structure in all cases. While the two bottommost targets with equal amounts of organic and inorganic components are both phase pure, the two uppermost targets with an increased organic portion contain foreign phases that are mostly related to FAI and MAI.

Using the (002)-reflection for the two bottommost targets, lattice constants of 6.256(1) Å for MASI and 6.279(1) Å for MAFASI are calculated. Other groups reported values of 6.241–6.246 Å and 6.318 Å [12, 51], respectively. It is worthwhile to mention that these results were obtained with crystals or powders that were fabricated by very different methods, often employing additives like H_3PO_2 or SnF_2. Thus, the MA-based perovskite we fabricated from the pure powders by solid-state reaction reveals a slightly modified cubic lattice. As a consequence of the integration of the smaller MA cations into the FA sublattice, the mixed perovskite reveals an intermediate lattice parameter between the pure substances.
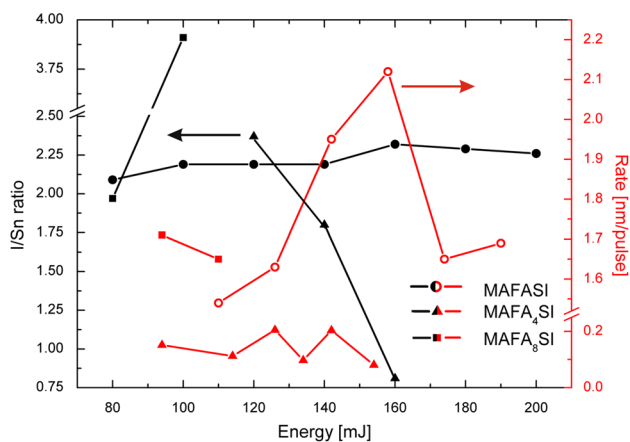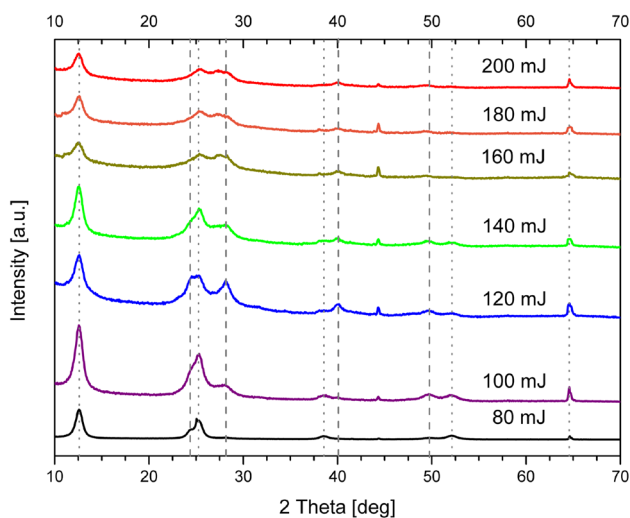
3.2 Thin films

3.2.1 Chemical composition

As described above, a suitable process window for thin film deposition has to be identified, where the laser fluence is of the utmost importance.

When the fluence is increased, more and more target material is ablated; hence, the rate is increasing. Above a certain value, the Knudsen-layer formed by evaporated material is (partially) shielding the target [41]; therefore, the ablation is inefficient and the rate decreases again. Similarly, the amount of the organic part is reduced for high fluences. Here, the higher density of the ablated component [46] results in a broadening of the angular distribution of the plasma due to multiple collisions [50]. Since this is, in particular, true for the lighter species, they are scattered to larger angles and do not contribute to the film growth. Likewise, for the intense laser beam the degree of ionization is enhanced [37, 47], leading to a pronounced damage of the organic molecules [49]. Hence, the more volatile organic fragments are lost during plasma expansion. Furthermore, high fluences can induce the decomposition of the target (compare Fig. 1c) and this way a depletion of the organic component.

In coincidence with the deposition rate, the highest composition is measured for a laser energy of 160 mJ for MAFASI, although there is still a considerable lack of the organic compound (Fig. 3). From these results, we draw the conclusion that as a matter of principle the organic-to-inorganic ratio of the target cannot be transferred to a thin film under any combination of deposition parameters (substrate temperature, fluence, gas pressure and target-to-substrate distance) due to the mechanisms mentioned above, and

Fig. 2 Diffractograms of four different targets. Labeled peaks are assigned to the planes of a cubic perovskite lattice (space group Pm$\bar{3}$m, no. 221). Note that only the most intense peaks are indexed for reasons of clarity and that the intensities are plotted in linear scaling

Fig. 3 Ratio of iodine to tin (black symbols) and deposition rate (red symbols) as a function of the energy density for MAFASI, MAFA$_4$SI and MAFA$_8$SI thin films

Fig. 4 Diffractograms of MAFASI thin films deposited at various energies, ranging from 80 to 200 mJ. The dotted lines indicate the positions of [001]-reflections of α-SnI$_2$ [39], while the dashed ones indicate the (111), (002), (022) and (222)-lattice planes of the perovskite structure from left to right, respectively. Note that the intensities are plotted in linear scaling

hence, a target with an unequal composition of both species has to be used.

The targets enriched in the organic component also reveal maxima in the I/Sn ratio and the deposition rate, although not at the same value of the fluence. While for the fourfold amount of MAFA, the ideal stoichiometry of 3:1 is still not reached, it can even be exceeded for MAFA$_8$SI.

3.2.2 Phase composition

Whether the perovskite structure can be built despite organic deficiency is analyzed using the example of MAFASI by recording diffractograms of thin films deposited at room temperature using different energies from 80 to 200 mJ (Fig. 4), the diffractograms are dominated by the [001]-reflections of SnI$_2$ (dotted lines). In spite of the organic deficiency, a polycrystalline perovskitic phase is formed at room temperature, namely in (111), (002), (022) and (222) orientation (dashed lines). The intensities of the perovskite peaks are most pronounced at 120 mJ. As mentioned before for higher energies, especially the volatile organic fragments are lost during the deposition process. Hence, less material is available to form the perovskite phase and surplus inorganic species can be found. For lower fluences, we assume that the energy of the particles during nucleation is not sufficient to form the MAFASI complex but the more simple SnI$_2$ crystallites. The film at 120 mJ shows a high degree of crystallinity of 90.6%, while 43.0% is attributed to the perovskite, 41.8% to SnI$_2$ and 5.8% to foreign phases, respectively. The value of the lattice parameter of the perovskite is 6.342(1) Å, again calculated from the (002)-reflection. To our knowledge, lattice constants of laser deposited MAFASI thin films have not been reported so far.

For MAFA$_4$SI and MAFA$_8$SI, the same effects are observed, while the energy densities resulting in the most pronounced perovskite portion are 120 mJ and 100 mJ, respectively.

3.2.3 Surface morphology and crystallinity

Since the process windows for film deposition is identified, the crystal structure and morphology of the films are investigated next.

For every target, the energy density for thin film deposition is chosen according to the highest Sn/I ratio (see Fig. 3). The corresponding thin films are depicted in Fig. 5. Comparing the areas of the crystalline peaks in (a), it becomes apparent that MAFASI contains equivalent portions of the perovskite and SnI$_2$ phases and that in the case of MAFA$_8$SI, the latter is significantly decreased to half of the perovskite amount, whereas for MASI and MAFA$_4$SI the diffractograms are dominated by SnI$_2$ reflections and foreign phases. We relate the underperforming of MAFA$_4$SI in view of perovskite growth to its minor amount in the target (see Fig. 2). MASI is expected to be less stable than the mixed cation halides giving rise to the almost complete deterioration of the perovskite structure.

For MASI and MAFASI films in Fig. 5b, c, the grain size of the crystallites is below 10 nm for all species; hence, the surface appears homogeneous and laminary covered, which is very likely to be related to the high SnI$_2$
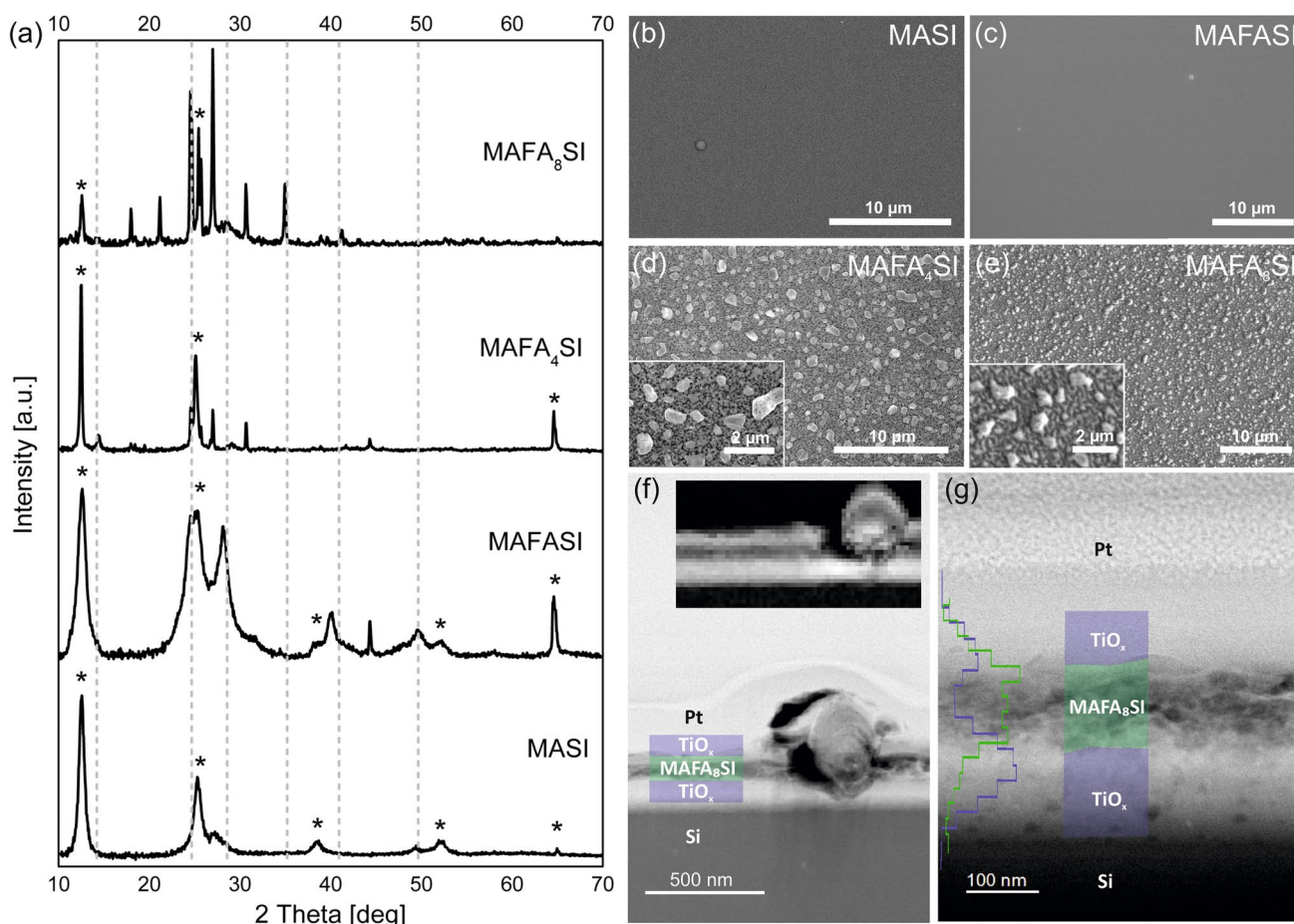
Fig. 5 Thin films deposited from all targets. **a** XRD scans with asterisk (*) denoting the SnI_2 phase [26] and dashed gray lines, the positions of the perovskite peaks. **b–e** SEM surface images of the films reveal thicknesses of 280 nm, 975 nm, 250 nm and 514 nm and were deposited at 130 mJ, 120 mJ, 120 mJ and 100 mJ. In **d, e** detailed views are shown. **f** Overview ADF-STEM image of a cross section through a $TiO_x/MAFA_8SI/TiO_x$ multilayer stack. In the inset, an EELS measurement of the integrated Ti L-edge after power-law background subtraction is depicted. **g** Enlarged view on the perovskite layer with spatially resolved intensities of EDX line scans of Ti K_α (blue) and Sn L_α (green). Note that the intensities are normalized

content. Indeed due to charging effects, the grain boundaries cannot be depicted. In the SEM images, droplets and/or exfoliations, respectively, can be identified as bright spots. They were chosen on purpose to demonstrate the good focus on the surface. The MAFASI films are just as smooth as the MASI ones even though the thickness is increased by a factor of three. According to the lack of organic species, the least amount of perovskitic phase is formed. Since this is particularly evident for MASI, the stabilizing effect of FA is explicitly demonstrated. The addition of FA ions entails a minimized oxidation of Sn^{2+} to Sn^{4+} which is attributed to the formation of Sn^{2+} vacancies in the perovskite lattice [17, 35]. This is the consequence of the larger ionic size of FA, leading to higher formation energies of Sn vacancies [43].

The over-stoichiometric films (d,e) show a very different behavior, and here, micron-sized islands are embedded in a granular matrix. For MAFA_4SI, the grains in the underlying film reveal sizes of approximately 100 nm and for the MAFA_8SI film of doubled thickness, they are twice as large in average with a few exceptions with diameters up to 600 nm. Consequently, in the detailed views two stages of thin film growth can be identified: island formation with islands and voids of the same size (d) and coalescence where the grains are separated by grain boundaries (e).

For comparison, with solvent-based preparation methods, the fast crystallization of tin-based perovskites is the determining factor for crystal growth limiting the grain size to 300 nm [30] without anti-solvent additives.

In the annular dark-field TEM image (f), a cross section of a $TiO_x/MAFA_8SI/TiO_x$ multilayer stack on a Si substrate is shown with a titanium oxide droplet on the right side of the image that impinged on the specimen during the deposition of the first layer and was than covered by the perovskite
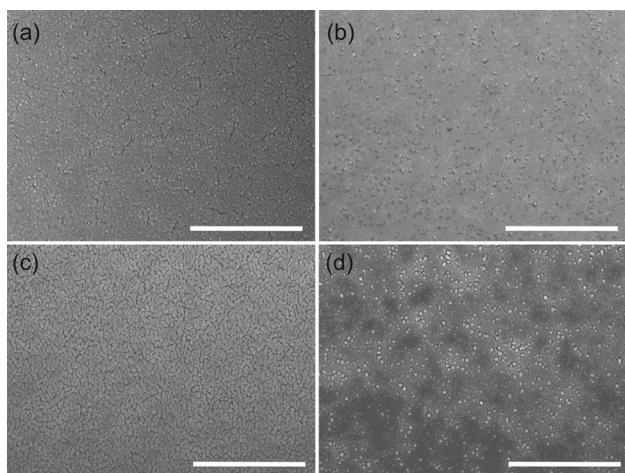
and second titanium layer. This is evidenced by the EELS measurement at the Ti L-edge in the inset. An enlarged view on the multilayer is depicted in (g). The oxide layers appear homogeneous, while the perovskite layer is textured but compact and reveals a wavy surface. Normalized line scans summing up the intensities of the Ti K_α at 4.51 keV (blue) and Sn L_α at 3.44 keV (green) EDX signals in the horizontal direction show that due to the impact of the heavier TiO_x clusters, the intermixing zone of the two layers is more extended compared to the interface of the perovskite growing on the oxide. Due to thinning of the lamella and the reduced layer thickness as a result of the pronounced intermixing, the signal of the topmost oxide layer is weaker than the other oxide layer.

An absorber layer in solar cells typically reveals a thickness of a few hundreds of nanometers. Nevertheless, the films have to be compact which, in particular, means void-free. An approach to facilitate this is to improve the coverage by enhancing the deposition temperature or to further increase their thickness.

3.2.4 Elevated temperature studies

Since the MASI films are most prone to humidity-induced degradation and the fraction of the perovskite phase in thin films is low, we focus on the mixed-cation variant to investigate the optimization potential of thin films by depositing at elevated temperatures or rather the resilience of initially smooth films against exposure to these temperatures, again using the example of MAFASI.

The films in Fig. 6 were deposited at 160 mJ and reveal slightly higher thicknesses referring to the films presented before of about 1 μm (a, c) and 600 nm (b, d), in order to strengthen the visibility of structural changes and to simultaneously gain information about the impact of the layer thickness. Starting at 60 °C (a), the crystallites are separated by crack-shaped voids and pinholes. When the temperature is increased, the crystallites are even more detached. Hence, growing thicker films do not lead to an improvement in the homogeneity at all.
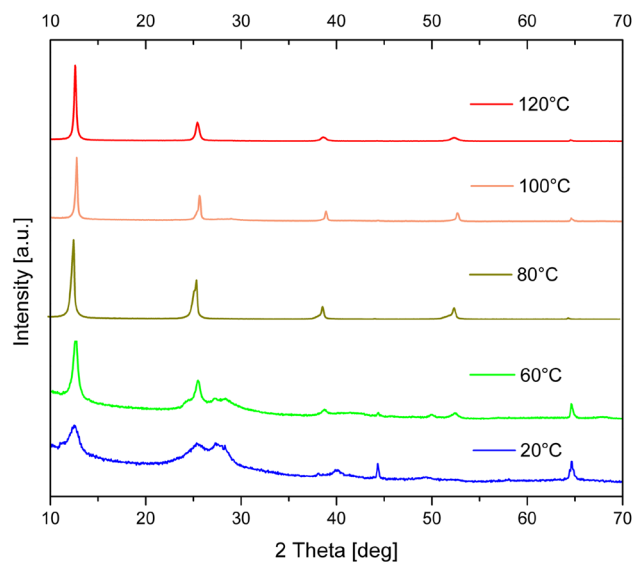
At 80 °C for a thinner layer, no cracks are found, but isolated islands on top of the film, while the latter appears to be very smooth. The higher the temperature, the more islands of roundish shape occur, this way destroying the film. Annealing films at temperatures below 80 °C may indeed help to improve quality.

This was checked using X-ray diffraction. The ratio of SnI_2 to perovskite is continuously deteriorating when comparing surface area of the peaks as the temperature is raised (see Fig. 7). Therefore, the crystallites in Fig. 6 are most likely to consist of a tin-rich phase. Exceeding 80 °C, only pure SnI_2 is detected.

3.3 Optical properties

3.3.1 Ellipsometry

After structural characterization, the films are inspected with regard to their optical properties and hence suitability as absorber layers in solar cells. Employing ellipsometry, all four perovskite materials are characterized and optical models on basis of a two-term Forouhi–Bloomer function are built. Therefore, direct fitting of the band gaps is not possible due to their twofold usage in the model. Instead, fixed numbers between 0.5 and 2.0 eV are utilized and the

Fig. 6 SEM images of MAFASI films at different substrate temperatures **a** 60 °C, **b** 80 °C, **c** 100 °C and **d** 120 °C. Scale bars denote 10 μm

Fig. 7 Diffractograms of MAFASI thin films, deposited at 120 mJ and various temperatures, ranging from room temperature to 200 °C
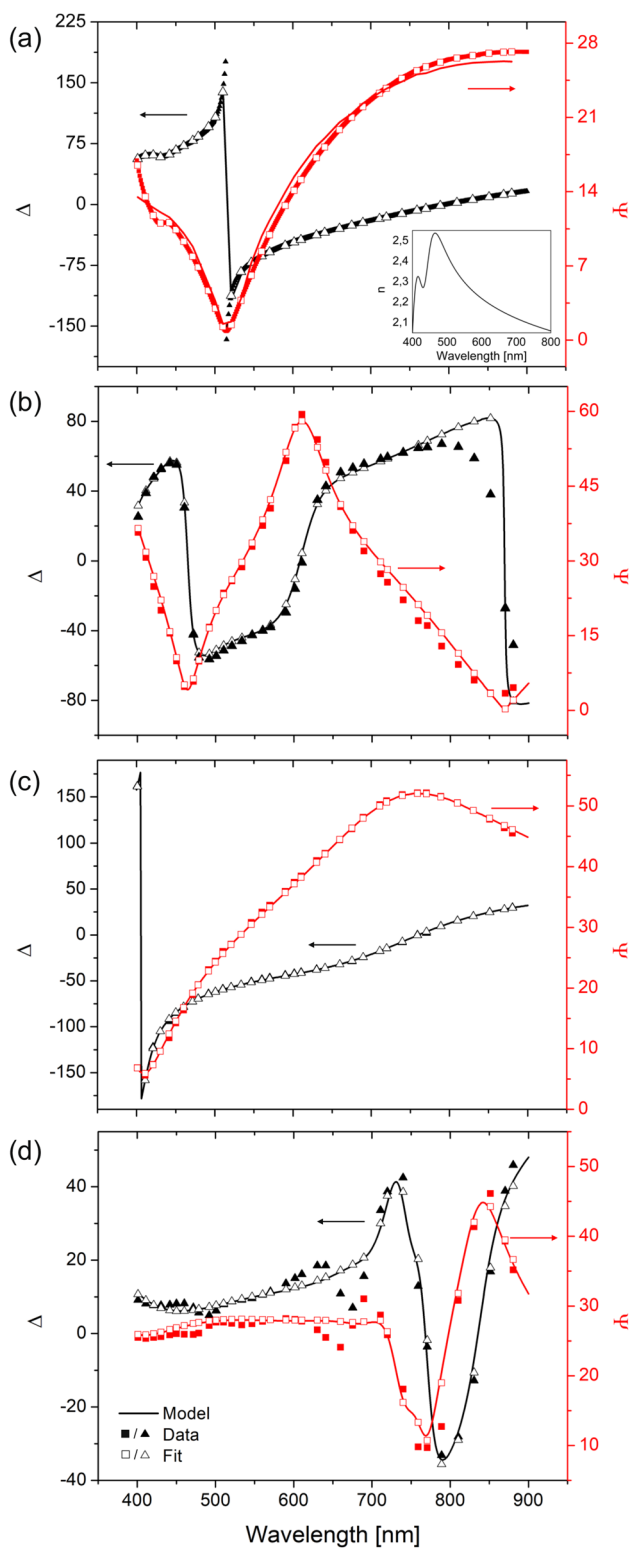
Fig. 8 Ellipsometric observables Δ and Ψ as a function of the wavelength for **a** MASI (91 nm), **b** MAFASI (345 nm), **c** MAFA$_4$SI (125 nm) and **d** MAFA$_8$SI (342 nm). The measurement data are depicted as solid symbols, the build model as a solid line and the fit of the model to the data as open symbols. Additionally in **a** the refractive index is shown as a function of wavelength

least deviation of fit, data and model is applied as a quality criterion to determine the value of the band gap. This is expressed by the root mean square error (RMSE) revealing values of 4.2, 8.7, 0.651 and 3.6, respectively (Fig. 8a–d), indeed above 800 nm for MAFASI the deviation of model and data increases, and hence, the RMSE value is notably larger.

The curve of the refractive index as a function of the wavelength for MASI (a) reveals a characteristic shape that is also documented by other groups [1]. In detail, the value is in the range of 2.0–2.6 and the function is decaying toward larger wavelengths after passing a local minimum first.

In Table 2, the results gained in this work are listed together with values documented in the literature. For MASI and MAFASI, we find our results in excellent agreement with the reported values. The band gaps of the organic-rich MAFA$_4$SI and MAFA$_8$SI reveal values close to MAFASI, the perovskite in ideal stoichiometry.

Table 2 Values for the indirect band gap in perovskites

Composition	References	Band gap (eV)
MASnI$_3$	[17, 44]	1.20–1.30
MASnI$_3$	This work	1.30
MA$_{0.2}$FA$_{0.8}$SnI$_3$	This work	1.40
MA$_{0.25}$FA$_{0.75}$SnI$_3$	[19, 53]	1.33–1.40
(MA$_{0.2}$FA$_{0.8}$)$_4$SnI$_3$	This work	1.325–1.350
(MA$_{0.2}$FA$_{0.8}$)$_8$SnI$_3$	This work	1.375
FASnI$_3$	[21, 22, 25]	1.40–1.41
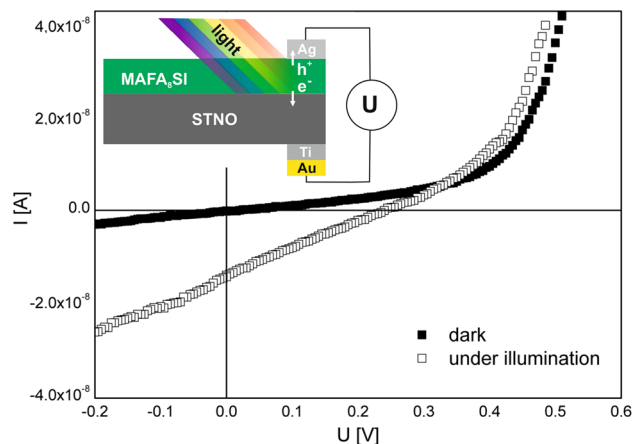
Fig. 9 Photovoltaic characterization. Current–voltage characteristic in the dark (solid squares) and under illumination with a Xe lamp (open squares). The inset shows a sketch of the sample geometry

3.3.2 Photovoltaic characterization

After verifying that the band gaps of the laser deposited perovskite layers are suitable for solar cells, a rudimentary version is tested in a photovoltaic measurement setup at room temperature. The sample is constructed of the essential parts only, consisting of the 400-nm-thick $MAFA_8SI$ absorber layer on a conductive substrate ($Nb:SrTiO_3$ (STNO) at 0.5 wt% Nb) and metal contacts (see inset in Fig. 9). The ohmic contacts on STNO with dimensions of 0.95×0.45 mm^2 are fabricated by means of sputter deposition through a shadow mask at room temperature, the top-contact by manually adding conductive silver paste. In two-point geometry, they are connected to a Keithley 2430, which serves as voltage source and amp meter, while the voltage drop between top and bottom electrodes is measured by a Keithley 2182A Nanovoltmeter. Polychromatic illumination near the top contact is provided by a xenon lamp at fixed power of 175 mW and a spot diameter of about 3 mm.

The current–voltage curves in Fig. 9 exhibit a rectifying behavior. For positive voltages, an almost exponential increase in current is detected, whereas the voltage dependency is only weakly pronounced in the negative voltage direction. In the dark, the curve passes the origin, while under illumination an offset toward negative currents is visible, demonstrating clearly the photovoltaic effect characterized by a short-circuit current $I_{SC} = 14$ nA and an open-circuit voltage $V_{OC} = 0.24$ V.

For $MA_{0.25}FA_{0.75}SnI_3$, a maximum value of $V_{OC} = 0.61$ V was documented [53], while the corresponding layer revealed a thickness of 150 nm and for thicker layers this value was notably reduced. For this type of perovskites, high carrier mobilities and diffusion lengths up to 550 nm (MASI) or 250 nm (FASI) are reported [31, 33]. Nevertheless, the thickness of approximately 400 nm chosen to ensure a complete coverage of the substrate in order to avoid leakage currents is definitely disadvantageous in view of device performance, due to the enhanced number of pinning centers in the form of defects or grain boundaries acting as recombination sites for the charge carriers, both scaling with the thickness.

Furthermore, due to the simplified measurement geometry no protection layers were employed to prevent or at least reduce the degradation of the perovskite. Although the deposition steps and the photovoltaic characterization are carried out in vacuum conditions, the transfer between the various facilities cannot be neglected, since the decomposition is happening on the minute-scale [34].

Despite the manifold drawbacks, the gained result in the absence of compact electron and hole transmitting layers for efficient charge transport, beyond that serving as protection layers, can be regarded as very promising.

4 Conclusions

In summary, we showed the manufacture of $\left[(NH_2CH)_{1-x}(CH_3NH_3)_x\right]_y SnI_3$ ($y = 1, 4, 8$ and $x = 1, 0.2$) PLD targets by means of solid-state reaction from the initial powders and the deposition conditions under which thin films can be grown using the variety of target compositions. Here, the usage of over-stoichiometric targets in regard to the organic component is motivated by the literature documented loss of volatile species during the deposition process, that is also in agreement with our findings. All films revealed perovskite structure at room temperature, where the thin film lattice constant of 6.342(1) Å is in good agreement with the bulk value for this system. The films grown from the organic rich targets revealed the highest perovskite fraction but were composed of a porous matrix and large crystallites. However, further annealing procedures do not reveal a purely positive effect on the morphology. Indeed, a tin-rich phase is formed, while the amount of the organic component is continuously decaying. The same effect is evident for high deposition energies. Though, for intermediate energies of 100–130 mJ and room temperature, smooth and homogeneous films with a high surface coverage were grown from MASI and MAFASI and likewise films with an enhanced portion of the perovskitic structure from $MAFA_8SI$, their optical properties were analyzed, revealing band gaps between 1.3 and 1.4 eV suitable for energy conversion in the visible spectrum. Additionally, the functionality of a simplified solar cell with a $MAFA_8SI$ absorber layer was demonstrated as well. Combining all the gained results, the fabrication of thin film hybrid organic–inorganic perovskite solar cells via PLD is a feasible approach, since it is enabled to specifically manipulate the film properties by tuning the deposition parameters. Hence, it is possible to address questions about the impact of certain variables as the grain size on the carrier diffusion length, which is only possible to a limited extent with other fabrication methods.

Compliance with ethical standards

Conflict of interest The authors declare that they have no conflict of interest.

References

1. M. Anaya, J.P. Correa-Baena, G. Lozano, M. Saliba, P. Anguita, B. Roose, A. Abate, U. Steiner, M. Grätzel, M.E. Calvo et al., Optical analysis of $CH_3NH_3Sn_xPb_{1-x}I_3$ absorbers: a roadmap for perovskite-on-perovskite tandem solar cells. J. Mater. Chem. A **4**(29), 11214–11221 (2016)

2. A. Babayigit, A. Ethirajan, M. Muller, B. Conings, Toxicity of organometal halide perovskite solar cells. Nat. Mater. **15**(3), 247 (2016)

3. T. Baikie, Y. Fang, J.M. Kadro, M. Schreyer, F. Wei, S.G. Mhaisalkar, M. Graetzel, T.J. White, Synthesis and crystal chemistry of the hybrid perovskite $(CH_3NH_3)PbI_3$ for solid-state sensitised solar cell applications. J. Mater. Chem. A **1**(18), 5628–5641 (2013)

4. U. Bansode, R. Naphade, O. Game, S. Agarkar, S. Ogale, Hybrid perovskite films by a new variant of pulsed excimer laser deposition: a room-temperature dry process. J. Phys. Chem. C **119**(17), 9177–9185 (2015)

5. U. Bansode, S. Ogale, On-axis pulsed laser deposition of hybrid perovskite films for solar cell and broadband photo-sensor applications. J. Appl. Phys. **121**(13), 133107 (2017)

6. A.T. Barrows, A.J. Pearson, C.K. Kwak, A.D. Dunbar, A.R. Buckley, D.G. Lidzey, Efficient planar heterojunction mixed-halide perovskite solar cells deposited via spray-deposition. Energy Environ. Sci. **7**(9), 2944–2950 (2014)

7. C. Bi, Y. Shao, Y. Yuan, Z. Xiao, C. Wang, Y. Gao, J. Huang, Understanding the formation and evolution of interdiffusion grown organolead halide perovskite thin films by thermal annealing. J. Mater. Chem. A **2**(43), 18508–18514 (2014)

8. A. Binek, F.C. Hanusch, P. Docampo, T. Bein, Stabilization of the trigonal high-temperature phase of formamidinium lead iodide. J. Phys. Chem. Lett. **6**(7), 1249–1253 (2015)

9. P.P. Boix, S. Agarwala, T.M. Koh, N. Mathews, S.G. Mhaisalkar, Perovskite solar cells: beyond methylammonium lead iodide. J. Phys. Chem. Lett. **6**(5), 898–907 (2015)

10. H.W. Chen, N. Sakai, M. Ikegami, T. Miyasaka, Emergence of hysteresis and transient ferroelectric response in organo-lead halide perovskite solar cells. J. Phys. Chem. Lett. **6**(1), 164–169 (2014)

11. J. Chen, N.G. Park, Causes and solutions of recombination in perovskite solar cells. Adv. Mater. **31**, 1803019 (2018)

12. Y. Dang, Y. Zhou, X. Liu, D. Ju, S. Xia, H. Xia, X. Tao, Formation of hybrid perovskite tin iodide single crystals by top-seeded solution growth. Angew. Chem. Int. Ed. **55**(10), 3447–3450 (2016)

13. F. de la Peña, E. Prestat, V.T. Fauske, P. Burdet, P. Jokubauskas, M. Nord, T. Ostasevicius, K.E. MacArthur, M. Sarahan, D.N. Johnstone, J. Taillon, A. Eljarrat, J. Lähnemann, V. Migunov, J. Caron, S. Mazzucco, T. Aarholt, M. Walls, T. Slater, F. Winkler, pquinn dls, B. Martineau, G. Donval, R. McLeod, E.R.

14. Q. Dong, Y. Yuan, Y. Shao, Y. Fang, Q. Wang, J. Huang, Abnormal crystal growth in $CH_3NH_3PbI_{3-x}Cl_x$ using a multi-cycle solution coating process. Energy Environ. Sci. **8**(8), 2464–2470 (2015)

15. G.E. Eperon, V.M. Burlakov, P. Docampo, A. Goriely, H.J. Snaith, Morphological control for high performance, solution-processed planar heterojunction perovskite solar cells. Adv. Funct. Mater. **24**(1), 151–157 (2014)

16. V. Goldschmidt, Krystallbau und chemische zusammensetzung. Berichte der deutschen chemischen Gesellschaft (A B Ser.) **60**(5), 1263–1296 (1927)

17. F. Hao, C.C. Stoumpos, D.H. Cao, R.P. Chang, M.G. Kanatzidis, Lead-free solid-state organic–inorganic halide perovskite solar cells. Nat. Photonics **8**(6), 489 (2014)

18. S.F. Hoefler, G. Trimmel, T. Rath, Progress on lead-free metal halide perovskites for photovoltaic applications: a review. Monatshefte für Chemie-Chem. Mon. **148**(5), 795–826 (2017)

19. N. Ito, M.A. Kamarudin, D. Hirotani, Y. Zhang, Q. Shen, Y. Ogomi, S. Iikubo, T. Minemoto, K. Yoshino, S. Hayase, Mixed Sn-Ge perovskite for enhanced perovskite solar cell performance in air. J. Phys. Chem. Lett. **9**(7), 1682–1688 (2018)

20. N.J. Jeon, J.H. Noh, W.S. Yang, Y.C. Kim, S. Ryu, J. Seo, S.I. Seok, Compositional engineering of perovskite materials for high-performance solar cells. Nature **517**(7535), 476 (2015)

21. Y. Jiang, A.M. Soufiani, A. Gentle, F. Huang, A. Ho-Baillie, M.A. Green, Temperature dependent optical properties of $CH_3NH_3PbI_3$ perovskite by spectroscopic ellipsometry. Appl. Phys. Lett. **108**(6), 061905 (2016)

22. W. Ke, C.C. Stoumpos, M. Zhu, L. Mao, I. Spanopoulos, J. Liu, O.Y. Kontsevoi, M. Chen, D. Sarma, Y. Zhang et al., Enhanced photovoltaic performance and stability with a new type of hollow 3D perovskite {en} $FASnI_3$. Sci. Adv. **3**(8), e1701293 (2017)

23. G.Y. Kim, A. Senocrate, T.Y. Yang, G. Gregori, M. Grätzel, J. Maier, Large tunable photoeffect on ion conduction in halide perovskites and implications for photodecomposition. Nat. Mater. **17**(5), 445 (2018)

24. H.S. Kim, N.G. Park, Parameters affecting I-V hysteresis of $CH_3NH_3PbI_3$ perovskite solar cells: effects of perovskite crystal size and mesoporous TiO_2 layer. J. Phys. Chem. Lett. **5**(17), 2927–2934 (2014)

25. T.M. Koh, K. Fu, Y. Fang, S. Chen, T. Sum, N. Mathews, S.G. Mhaisalkar, P.P. Boix, T. Baikie, Formamidinium-containing metal-halide: an alternative material for near-IR absorption perovskite solar cells. J. Phys. Chem. C **118**(30), 16458–16462 (2013)

26. V. Kostko, O. Kostko, G. Makovetskii, K. Yanushkevich, Thin film structure of tin (ii) iodide. Physica Status solidi (b) **229**(3), 1349–1352 (2002)

27. H.U. Krebs, M. Weisheit, J. Faupel, E. Süske, T. Scharf, C. Fuhse, M. Störmer, K. Sturm, M. Seibt, H. Kijewski, et al., Pulsed laser deposition (PLD)—A versatile thin film technique, in *Advances in Solid State Physics* (Springer, 2003), pp. 505–518

28. F. Lang, O. Shargaieva, V.V. Brus, H.C. Neitzert, J. Rappich, N.H. Nickel, Influence of radiation on the properties and the stability of hybrid perovskites. Adv. Mater. **30**(3), 1702905 (2018)

29. T. Lippert, UV laser ablation of polymers: from structuring to thin film deposition, in *Laser-Surface Interactions for New Materials Production* (Springer, 2010), pp. 141–175

30. J. Liu, M. Ozaki, S. Yakumaru, T. Handa, R. Nishikubo, Y. Kanemitsu, A. Saeki, Y. Murata, R. Murdey, A. Wakamiya, Lead-free solar cells based on tin halide perovskite films with high coverage and improved aggregation. Angew. Chem. **130**(40), 13405–13409 (2018)

Hoglund, I. Alxneit, D. Lundeby, T. Henninen, L.F. Zagonel, A. Garmannslund, hyperspy/hyperspy: v1.4.2 (2019). https://doi.org/10.5281/zenodo.3249885

31. L. Ma, F. Hao, C.C. Stoumpos, B.T. Phelan, M.R. Wasielewski, M.G. Kanatzidis, Carrier diffusion lengths of over 500 nm in lead-free perovskite $CH_3NH_3SnI_3$ films. J. Am. Chem. Soc. **138**(44), 14750–14755 (2016)

32. T. Matsushima, T. Fujihara, C. Qin, S. Terakawa, Y. Esaki, S. Hwang, A.S. Sandanayaka, W.J. Potscavage, C. Adachi, Morphological control of organic-inorganic perovskite layers by hot isostatic pressing for efficient planar solar cells. J. Mater. Chem. A **3**(34), 17780–17787 (2015)

33. R.L. Milot, M.T. Klug, C.L. Davies, Z. Wang, H. Kraus, H.J. Snaith, M.B. Johnston, L.M. Herz, The effects of doping density and temperature on the optoelectronic properties of formamidinium tin triiodide thin films. Adv. Mater. **30**(44), 1804506 (2018)

34. R. Nishikubo, N. Ishida, Y. Katsuki, A. Wakamiya, A. Saeki, Minute-scale degradation and shift of valence-band maxima of $CH_3NH_3SnI_3$ and $HC(NH_2)_2SnI_3$ perovskites upon air exposure. J. Phys. Chem. C **121**(36), 19650–19656 (2017)

35. N.K. Noel, S.D. Stranks, A. Abate, C. Wehrenfennig, S. Guarnera, A.A. Haghighirad, A. Sadhanala, G.E. Eperon, S.K. Pathak, M.B. Johnston et al., Lead-free organic-inorganic tin halide perovskites for photovoltaic applications. Energy Environ. Sci. **7**(9), 3061–3068 (2014)

36. J.H. Noh, S.H. Im, J.H. Heo, T.N. Mandal, S.I. Seok, Chemical management for colorful, efficient, and stable inorganic-organic hybrid nanostructured solar cells. Nano Lett. **13**(4), 1764–1769 (2013)

37. S. Rajendiran, A. Rossall, A. Gibson, E. Wagenaars, Modelling of laser ablation and reactive oxygen plasmas for pulsed laser deposition of zinc oxide. Surf. Coat. Technol. **260**, 417–423 (2014)

38. F. Sani, S. Shafie, H. Lim, A. Musa, Advancement on lead-free organic-inorganic halide perovskite solar cells: a review. Materials **11**(6), 1008 (2018)

39. Y. Sawada, M. Suzuki, Thermal change of SnI_2 thin films. Part 3. Isothermal change under light radiation. Thermochim. Acta **243**(1), 95–100 (1994)

40. P. Scajev, R. Aleksiejunas, S. Miasojedovas, S. Nargelas, M. Inoue, C. Qin, T. Matsushima, C. Adachi, S. Jursenas, Two regimes of carrier diffusion in vapor-deposited lead-halide perovskites. J. Phys. Chem. C **121**(39), 21600–21609 (2017)

41. J. Schou, Fundamentals of laser-assisted fabrication of inorganic and organic films, in *Functionalized Nanoscale Materials, Devices and Systems* (2008), p. 241

42. E.C. Schueller, G. Laurita, D.H. Fabini, C.C. Stoumpos, M.G. Kanatzidis, R. Seshadri, Crystal structure evolution and notable thermal expansion in hybrid perovskites formamidinium tin iodide and formamidinium lead bromide. Inorg. Chem. **57**(2), 695–701 (2017)

43. T. Shi, H.S. Zhang, W. Meng, Q. Teng, M. Liu, X. Yang, Y. Yan, H.L. Yip, Y.J. Zhao, Effects of organic cations on the defect physics of tin halide perovskites. J. Mater. Chem. A **5**(29), 15124–15129 (2017)

44. C.C. Stoumpos, C.D. Malliakas, M.G. Kanatzidis, Semiconducting tin and lead iodide perovskites with organic cations: phase transitions, high mobilities, and near-infrared photoluminescent properties. Inorg. Chem. **52**(15), 9019–9038 (2013)

45. S.D. Stranks, G.E. Eperon, G. Grancini, C. Menelaou, M.J. Alcocer, T. Leijtens, L.M. Herz, A. Petrozza, H.J. Snaith, Electron-hole diffusion lengths exceeding 1 micrometer in an organometal trihalide perovskite absorber. Science **342**(6156), 341–344 (2013)

46. B. Toftmann, J. Schou, T. Hansen, J. Lunney, Angular distribution of electron temperature and density in a laser-ablation plume. Phys. Rev. Lett. **84**(17), 3998 (2000)

47. G. Tyrrell, T. York, N. Cherief, D. Givord, J. Lunney, M. Buckley, I. Boyd, Kinetic energy and mass distribution of ablated species formed during pulsed laser deposition. Microelectron. Eng. **25**(2–4), 247–252 (1994)

48. F. Wang, J. Ma, F. Xie, L. Li, J. Chen, J. Fan, N. Zhao, Organic cation-dependent degradation mechanism of organotin halide perovskites. Adv. Funct. Mater. **26**(20), 3417–3423 (2016)

49. L. Wang, H. Kwok, Pulsed laser deposition of organic thin films. Thin Solid Films **363**(1–2), 58–60 (2000)

50. P. Willmott, J. Huber, Pulsed laser vaporization and deposition. Rev. Mod. Phys. **72**(1), 315 (2000)

51. K. Yamada, K. Fujise, S. Hino, Y. Yamane, T. Nakagama, Characterization of Sn (II)-based perovskites by XRD, DTA, NQR and ^{119}Sn NMR for photovoltaic applications. Chem. Lett. **48**(7), 749–752 (2019)

52. W.S. Yang, J.H. Noh, N.J. Jeon, Y.C. Kim, S. Ryu, J. Seo, S.I. Seok, High-performance photovoltaic perovskite layers fabricated through intramolecular exchange. Science **348**(6240), 1234–1237 (2015)

53. Z. Zhao, F. Gu, Y. Li, W. Sun, S. Ye, H. Rao, Z. Liu, Z. Bian, C. Huang, Mixed-organic-cation tin iodide for lead-free perovskite solar cells with an efficiency of 8.12%. Adv. Sci. **4**(11), 1700204 (2017)